Journal of Alloys and Compounds 509 (2011) 885–890

Contents lists available at ScienceDirect

Journal of Alloys and Compounds

journal homepage: www.elsevier.com/locate/jallcom

α-Fe_2O_3 nanoplates: PEG-600 assisted hydrothermal synthesis and formation mechanism

Guo-Ying Zhang*, Yan-Yan Xu, Dong-Zhao Gao, Ya-Qiu Sun

Tianjin Key Laboratory of Structure and Performance for Functional Molecules, College of Chemistry, Tianjin Normal University, Tianjin 300387, PR China

ARTICLE INFO

Article history:
Received 26 February 2010
Received in revised form
21 September 2010
Accepted 22 September 2010
Available online 1 October 2010

Keywords:
α-Fe_2O_3 nanoplates
PEG-600 polymer
Morphology control
Formation and growth mechanism
Optical property

ABSTRACT

Quasi-hexagonal α-Fe_2O_3 nanoplates with lateral sizes of 40–60 nm and thickness of ca. 10 nm were fabricated by a facile poly(ethylene glycol 600) (PEG-600) assisted hydrothermal technique in combination with calcination method. The final α-Fe_2O_3 nanoplates inherited perfectly the morphology of the preliminarily hydrothermal products with phases of dominant α-Fe_2O_3 and minor α-FeOOH. The platelets could be tailored from nano- to meso- and to micro-scale via adjusting PEG-600 quantities. An adsorption-extension-attachment model was proposed to explain the formation and growth mechanism of the platelets. The as-obtained α-Fe_2O_3 nanoplates exhibited a specific Langmuir surface area of 59 m^2/g and a maximum N_2 adsorption of 137.3 cm^3/g at 1 atm. UV–vis measurement showed a strong absorption in a wide range from UV to visible light with a blue-shifting band gap of 2.33 eV due to the nanosize effect.

1. Introduction

In recent years, there has been increasing interest in the synthesis of semiconductor nanoparticles with well-controlled size and shape, owing to their unique physical and chemistry properties which are useful in a wide application range such as catalysis, photonics and photoelectronics [1–3]. In particular, hematite (α-Fe_2O_3) is an important *n*-type semiconductor with excellent stability and nontoxicity under ambient conditions, and has been widely investigated in catalysts, gas sensors, photoelectrodes, magnetic devices, and lithium ion batteries [4–7]. It is reported that nanometer-sized particles can be grown into zero, one, two, and three dimensions (0, 1, 2, 3D) through various morphological control processes. By far a large variety of α-Fe_2O_3 nanostructures have been synthesized, including the most common 0D spherical nanoparticles [8], 1D nanocrystals such as wire [9], rod [10], spindle [11], and tube [12], 2D layered structure such as nanoflakes [13], and complex 3D architectures such as dendrite [14], urchin-like shapes [15], ordered columnar arrays [16], as well as core–shell hollow microspheres [17], and so on.

However, it is noted that most morphological control syntheses for α-Fe_2O_3 have mainly focused on the fabrication of 1D nanostructures [9–12] due to electric and thermal peculiarities on dimensionality and on the construction of interesting 3D high-complexity architectures [14–17]. In comparison, studies to induce formation of 2D nanoparticles such as nanodisks and nanoplates are still insufficient, which are considered to have potential applications in data storage, optics, and substrates for constructing nanodevices, as enlightened by other inorganic platelet materials with novel interesting properties [18,19]. Till now, few reports have addressed on the formation of 2D α-Fe_2O_3 nanostructures. Zhang et al. [20] fabricated quasi-circular α-Fe_2O_3 nanoplates through hydrothermal method using PEO20PPO70PEO20 (P123) triblock copolymer as template and citrate as complexing reagent. Yang's group [21] presented a citric acid-assisted hydrothermal process to produce hexagonal α-Fe_2O_3 with a lateral size of about 100 nm. Chowdari and co-authors [13] reported α-Fe_2O_3 nanoflakes prepared on Cu foil by using a thermal treatment method, which showed superior performance as anode material for Li-ion batteries.

Despite the few advances, however, it still remains a challenge to develop simple, low-cost and environment friendly approach to synthesize monodispersed α-Fe_2O_3 platelets with fine shape control as well as continuous diameter tuning. Hydrothermal process has been demonstrated to be an efficient synthetic pathway towards various size- and morphology-controllable nanostructures. Herein, we reported a facile poly(ethylene glycol 600) (PEG-600) assisted hydrothermal and post-heated approach for the fabrication of quasi-hexagonal α-Fe_2O_3 nanoplates with tunable average diameters from nano- to micro-scale with enhanced PEG-600 quantity. An adsorption-extension-attachment (AEA) model was proposed to explain the formation and growth mechanism of

* Corresponding author. Tel.: +86 22 23766515; fax: +86 22 23766532.
E-mail address: gyzhangtj@yahoo.cn (G.-Y. Zhang).

0925-8388/$ – see front matter © 2010 Elsevier B.V. All rights reserved.
doi:10.1016/j.jallcom.2010.09.124

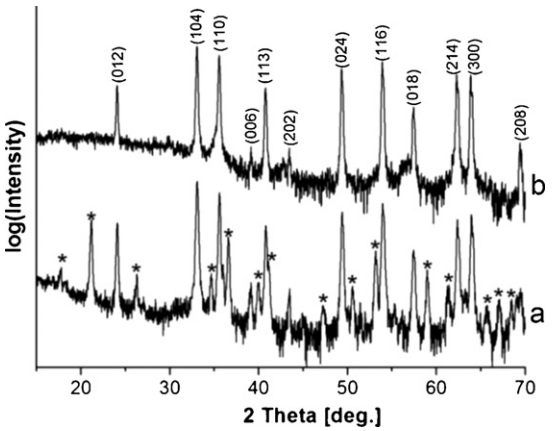

Fig. 1. XRD patterns of (a) hydrothermal sample synthesized with 5 mL of PEG-600 and (b) final product after calcination at 250 °C for 0.5 h.

α-Fe_2O_3 platelets. UV–vis optical property of α-Fe_2O_3 nanoplates with diameter of about 70 nm and lateral size of 40–60 nm showed an absorption band gap of 2.33 eV, blue-shifted in contrast to bulk hematite due to the quantum size effect. The results may imply potential applications in areas such as gas sensor, catalyst.

2. Materials and methods

2.1. Synthesis of α-Fe_2O_3 nanoplates

All the chemical reagents were of analytical grade and were used as received without further purification. In a typical synthesis, 0.3 mmol $Fe(NO_3)_3{\cdot}9H_2O$ was dissolved in 10 mL of deionized water, into which 5 mL of PEG-600 was subsequently introduced under fiercely magnetic stirring. Then, adequate amount of 6 M NaOH was dropped into the solution to adjust the pH to 8. After stirring for 30 min, the mixture was transferred into a 20 mL Teflon-lined autoclave, heated to 150 °C with a typical heating rate of 1.5 °C/min, and then maintained at the target temperature for 12 h. After the reaction was completed, the resulting solid precursor were centrifugated, washed sequentially with deionized water and ethanol repeatedly to move the residual reactants, and dried at 60 °C in air for 12 h. Finally, α-Fe_2O_3 nanoplates with high purity were harvested by heating the as-obtained precursor in air at 250 °C for 0.5 h. Contrast experiments were carried out by using 0, 10, and 15 mL of PEG-600 as additive, respectively.

2.2. Characterization and apparatus

The as-obtained samples were characterized by X-ray power diffraction (XRD) on a Japan Rigaku D/max-2500 X-ray diffractometer with graphite monochromatized Cu Kα1 (λ = 1.5405 Å) radiation at a scanning speed of 4°/min in 2θ ranging from 3° to 80°. Scanning electron microscopy (SEM) images were taken using a JEOL JSM-6700F microscope. Transmission electron microscopy (TEM) and high-resolution TEM (HRTEM) analyses were carried out under a JEOL JEM-2100 microscope operating at an accelerating voltage of 200 kV. IR spectra were measured on a TENSOR 27 (Bruker) FT-IR spectrometer with KBr pellets in the range 4000–400 cm^{-1}. N_2 adsorption isotherms for pressures in the range 0–1.0 bar were measured by a volumetric method using a Micromeritics ASAP2020 instrument. UV–vis diffuse reflectance spectra were recorded at room temperature on a JASCO V-550/V-570 UV–vis spectrophotometer fitted with an integrating sphere diffuse reflectance accessory.

3. Results and discussion

Fig. 1 shows the typical diffraction patterns of the hydrothermal sample in the presence of 5 mL of PEG-600 and the post-heat-treated final product. The reflections of the XRD pattern in Fig. 1a were attributed to a dominate phase of hexagonal α-Fe_2O_3 (JCPDS-ICDD Card No. 33-0664) mixed by a small quantity of α-FeOOH (JCPDS 29-713) with diffraction peaks emerged at the positions marked with stars. After the hydrothermal sample was calcined at 250 °C for 0.5 h, as shown in Fig. 1b, all the reflection peaks could be well indexed to hexagonal α-Fe_2O_3 with lattice constants a = 5.035 Å and c = 13.748 Å, in good agreement with the standard values. To clearly prove the purity of the final product, the intensity (y-axis) in Fig. 1 has been plotted in a log scale. No other characteristic peaks of impurities were observed in Fig. 1b, illustrating the high purity of the final α-Fe_2O_3 products. The XRD results demonstrated that the transformation from mixed α-Fe_2O_3 and α-FeOOH to pure α-Fe_2O_3 is easily achieved by heating at a low temperature of 250 °C for a short time of 0.5 h, which is beneficial to morphology maintenance of the products.

Fig. 2a and b displays the representative FE-SEM images of the final α-Fe_2O_3 sample at different magnifications. As shown by the panoramic view image in Fig. 2a, the product consists of a large quantity of nanoplates with a narrow size distribution. A magnified SEM image with marked arrows (Fig. 2b) describes that many nanoplates exhibit hexagonal or quasi-hexagonal morphology with a lateral size of ca. 40–60 nm and a thickness of ca. 10 nm. Moreover, the average diameter from one lateral to the opposite one was obtained by measuring the sizes of 100 randomly selected nanoplates. The histogram of the nanoplate diameter distribution (Fig. 2c) clearly indicates that the quasi-hexagonal α-Fe_2O_3 nanoplates have a relatively centralized diameter range of 60–80 nm with an average diameter of 71.3 ± 2.8 nm. The detailed morphology and microstructure of the α-Fe_2O_3 nanoplates were further characterized by TEM and HRTEM. From the typical TEM image in Fig. 2d, quasi-hexagonal platelike morphology with considerably uniform size can be obviously seen, in good accordance with the SEM results. Fig. 2e gives an enlarged TEM image of an individual nanoplate with lateral length of ca. 35 nm. The inset shows the corresponding fast Fourier transform (FFT) pattern, indicating the single crystalline nature of the α-Fe_2O_3 nanoplate. From the HRTEM image of the marked area of the nanoplate in Fig. 2e, the lattice fringes with an interplanar distance of 3.67 Å can be clearly seen, which is corresponding to the d-spacing of the (0 1 2) crystal planes. In addition, other platelets have also been observed by HRTEM and shows single crystal characteristics with lattice stripes of (1 0 4) and (1 1 3), respectively (Supporting information, Fig. S1), indicating the random growth directions of the platelets.

To learn more about the as-designed strategy, PEG-600 quantity dependent experiments were conducted. The results (Fig. 3) indicate that PEG-600 quantities have a great effect on the structure and morphology of hydrothermal products. In the absence of PEG-600, as shown in Fig. 3a, the sample presents multishape including irregular particles, platelets, and even rods with small aspect ratio. The corresponding XRD reflections are indexed to blended phases of major α-FeOOH and minor α-Fe_2O_3 as marked with squares. When 5 mL of PEG-600 is used in the reaction system, the product (Fig. 3b) is nanoplates with phase composition of dominant α-Fe_2O_3 and less α-FeOOH as described above in Fig. 1. The conformability of SEM images in Figs. 3b and 2b indicates good morphology maintenance after heat treatment. As PEG-600 is increased to 10 mL, the hydrothermal products (Fig. 3c) have grown up to irregular mesoplate of 200–800 nm with enhanced proportion of major phase α-Fe_2O_3. While in the presence of 15 mL of PEG-600, the nearly solvothermal process produces quasi-hexagonal microplates (Fig. 3d) with much larger lateral size of 2–3 μm and thickness of 200–400 nm. And the corresponding XRD pattern has changed to quasi-amorphous Fe_3O_4 (JCPDS 82-1533) mixed by α-Fe_2O_3.

As indicated by the XRD patterns in Fig. 3a–c, increased quantities of PEG-600 favor the formation of main phase α-Fe_2O_3. It has been proven that in a surfactant-free system, hydrothermal treatment of Fe^{3+} involves a two-step process of a primary hydrolysis to FeOOH and a subsequent dehydration to Fe_2O_3 [22]. In our strategy the nonionic polymer PEG-600 with plenty of hydrophilic –O– sites on the long chains could coordinate with Fe^{3+} to form ferrite glycolates [23], which would directly transform into Fe_2O_3 nanocrystals through dehydration under hydrothermal conditions [24] as the process related to a sol–gel route. Therefore, it is reasonable that

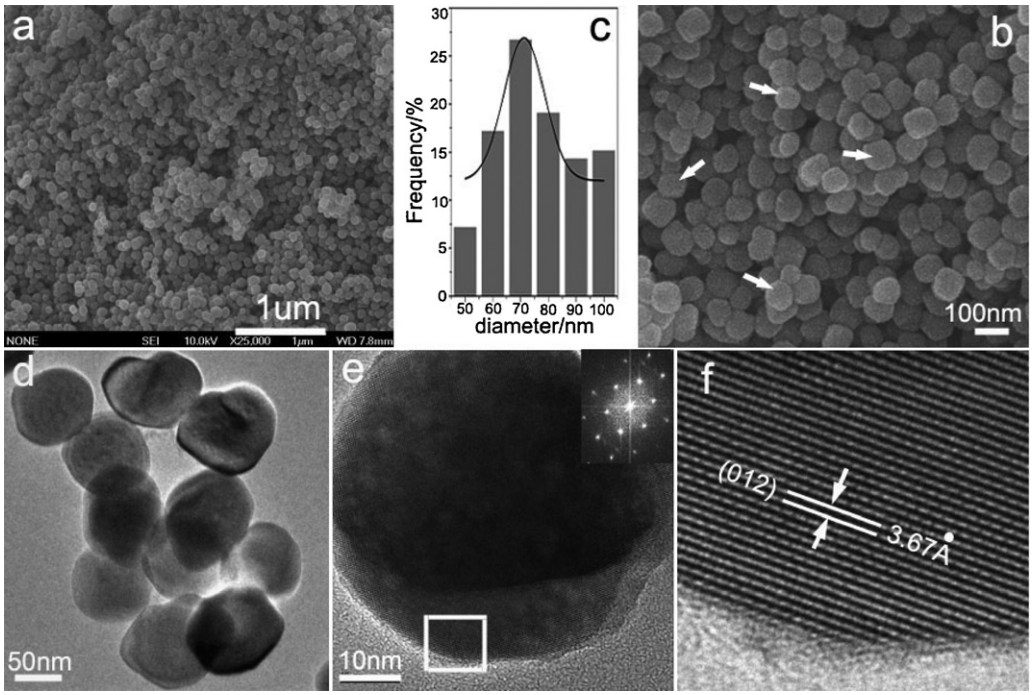

Fig. 2. Morphological and micro-structural characterization of α-Fe_2O_3 nanoplates. (a) Panoramic FE-SEM image, (b) magnified FE-SEM image, (c) the statistic histogram of the diameters distribution, (d) TEM image of several nanoplates, (e) TEM image of an individual nanoplate and inserted FFT pattern, and (f) HRTEM image taken from the marked square of the single nanoplate in e.

the proportion of α-Fe_2O_3 in hydrothermal products increases with PEG-600 quantities from 0 to 5 to 10 mL. But as excess PEG-600 of 15 mL is used, the typical reflections of α-FeOOH have vanished (Fig. 3d) and quasi-amorphous Fe_3O_4 forms simultaneously, which could be ascribed to the intrinsically reductive nature of the polyglycol [25].

As shown by the SEM images in Fig. 3a–d, the products can be tailored among "irregular particles-nanoplates-mesoplates-microplates" via adjusting the quantity of PEG-600. As mentioned above, the presence of PEG-600 benefits the formation of α-Fe_2O_3 nuclei, which belong to hexagonal syngony with lattice constants $a = b \neq c$. The two-dimensional (2D) quasi-hexagonal plate structure could be attributed to the selective adsorption and inhibition of PEG-600 on the *c*-axis of the freshly formed α-Fe_2O_3 nuclei. And the "nano- to meso- to micro-plate" process in Fig. 3b–d may be elucidated by an adsorption-extension-attachment model on the plate lateral as schematically demonstrates in Fig. 4.

The polyglycol PEG-600 has long chains with a high degree of flexibility. According to Xie and co-authors [26], a good solvent for PEG favors a full extension of the polymer chains, while a poor solvent favors the curl and twist of the chains. PEG-600 exhibits good solubility in water, so the chains should mainly present extension in our synthetic system. Furthermore, abundant hydrogen-bonds between adjacently extended PEG molecular chains and strong coordination of active oxygen with metal ions together contribute to the formation of thermodynamically stable multilayer interchains of Fe-complex (Fig. 4), which could adsorb on the lateral planes of initially formed α-Fe_2O_3 nuclei. More hematite nanoparticles with high surface activity would be generated via further hydrolysis of the multilayered Fe-complex and aggregate on the primary nuclei through a well-known "oriented attachment" mechanism [27] (Fig. 4). The driving force of this crystallization principle is that the elimination of the pairs of high energy surfaces will lead to a substantial reduction in the surface free energy from the thermodynamic viewpoint. And this crystallization mode offers special advantage of producing defect-free single crystals over classical crystallization [28]. Accordingly, increased PEG quantity benefits a broader extension of interchain Fe-complex and resultant more nuclei to form larger α-Fe_2O_3 plates as shown in Fig. 3b–d.

It should be stated that the above explanation about the formation and growth of the special platelet structures is somewhat conjectural and phenomenological. To verify the adsorption and coordination of PEG-600 to Fe^{3+}, FTIR absorption of hydrothermal product was measured (Supporting information, Fig. S2). In the spectrum, except the characteristic absorptions of Fe–O vibration in α-Fe_2O_3 and FeOOH (474, 567, 895 cm^{-1}) [29,30], and –OH stretching and bending vibration in residual PEG and adsorbed water (3426, 1631 cm^{-1}), the peak at 1091 cm^{-1} can be well assigned to C–O stretching vibration coordinating to metal cations. The shift to lower wavenumbers compared to pure PEG suggests the formation of chemical bonds between PEG and the inorganic components [31].

In view of the similar phase composition of the hydrothermal samples in Fig. 3a–c, α-Fe_2O_3 irregular particles and nano-/mesoplates were selected to investigate N_2 adsorption–desorption properties and the typical surface data were summarized in Table 1. It shows that α-Fe_2O_3 nanoplates exhibit the maximum surface area and the narrowest pore size distribution, while the irregular particles have a widest pore size distribution of 11–34 nm. In particular, the N_2 adsorption–desorption isotherms of α-Fe_2O_3 nano-/mesoplates are shown in Fig. 5a and b, respectively. And the insert displays the corresponding BJH pore size distribution calculated from the adsorption branch. The two samples both exhibit

Table 1
The typical surface data of different α-Fe_2O_3 samples.

Sample	Irregular particles	Mesoplates	Nanoplates
BET surface area (m^2/g)	36	11	44
Pore size distribution (nm)	11–34	10–18	11–13
Pore center (nm)	12, 25	12	12

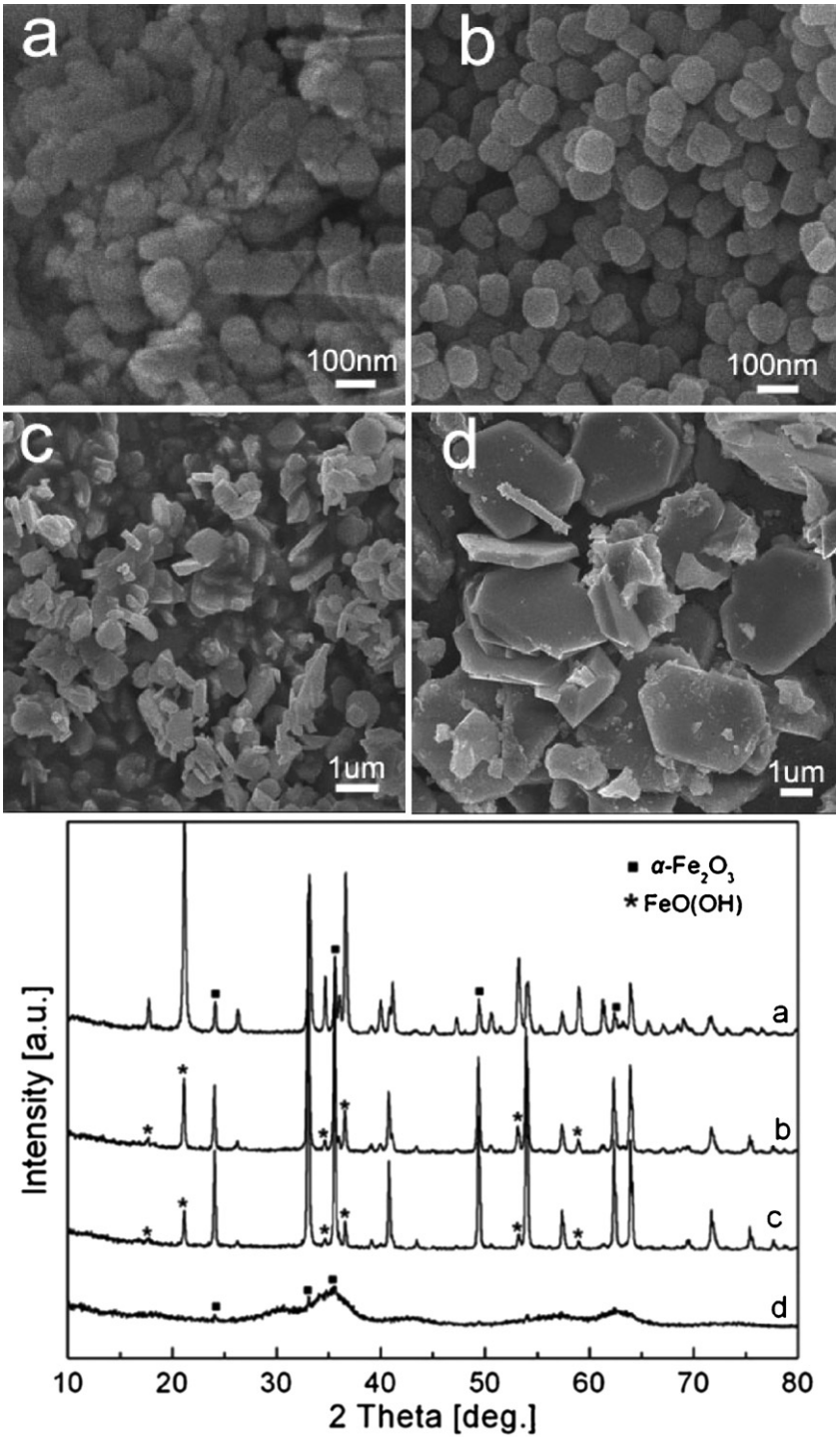

Fig. 3. FE-SEM images and XRD patterns of the precursor products prepared with different quantities of PEG-600: (a) 0 mL, (b) 5 mL, (c) 10 mL, and (d) 15 mL.

type-IV isotherms with a hysteresis loop in the relative pressure range of 0.8–1.0, indicating the presence of inhomogeneous mesopores, which are resulted from the aggregation of the plates [32]. The nanoplates (Fig. 5a) have a specific Langmuir surface area of 59 m^2/g and a BET surface area of 44 m^2/g, respectively, with a pore diameter range of 11–13 nm and a center at ca. 12 nm. And the maximum adsorption at approximately 1 atm. is 137.3 cm^3/g. In comparison, the Langmuir and BET surface areas of the mesoplates (Fig. 5b) are simply 15 and 11 m^2/g, respectively. Additionally, it displays an uneven pore size distribution from 10 to 18 nm and a significantly decreased maximum adsorption of 27 cm^3/g. The results preliminarily indicate that materials with smaller particle sizes have relatively higher surface area. And the sequence of reduced pore size distribution from irregular particles to meso- and to nanoplates shows that narrow size distributed product tends to aggregate into much more even mesopores.

Nanostructured materials usually exhibit blue-shifted phenomena in optical properties compared with the bulk counterparts. To reveal the electronic structure and size effect, UV–vis absorption measurement of the as-prepared α-Fe_2O_3 nanoplates was conducted at room temperature. According to the literatures [33–35], two absorption regions are expected in 200–600 nm. And

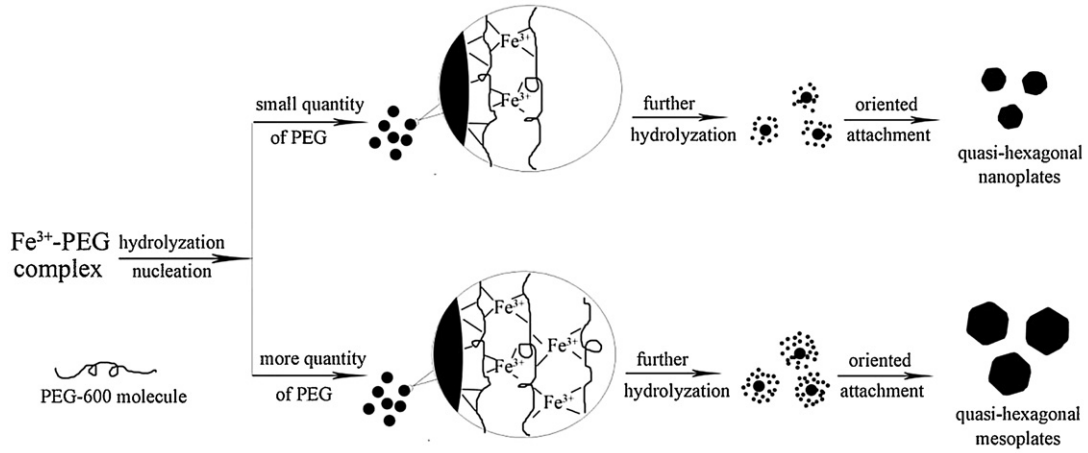

Fig. 4. Schematic illustration of the adsorption-extension-attachment model for the formation and growth mechanism of α-Fe_2O_3 platelets.

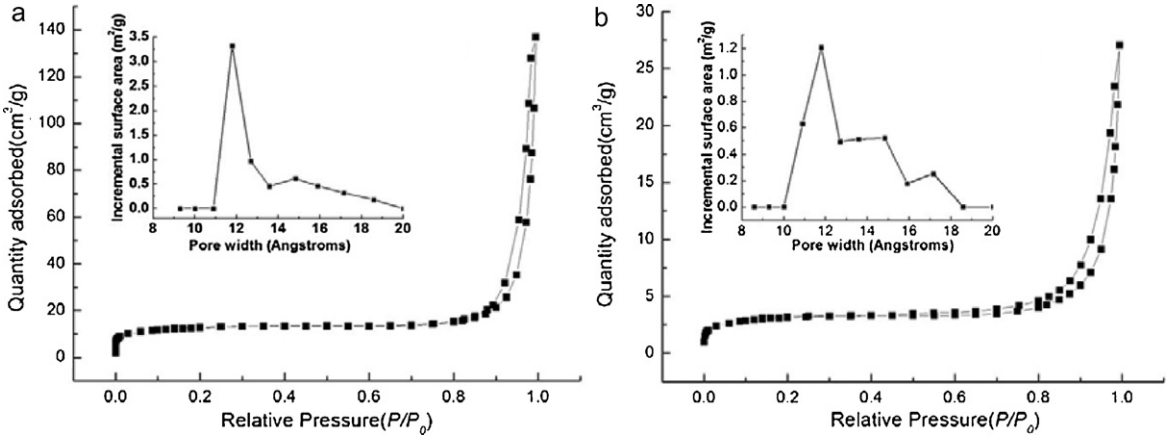

Fig. 5. N_2 adsorption–desorption isotherm of as-prepared α-Fe_2O_3 sample and the inserted BJH pore size distribution curve. (a) Nanoplates prepared with 5 mL of PEG-600 and (b) mesoplates prepared with 10 mL of PEG-600.

in our spectral experiment (Fig. 6), the obvious absorption of 250–350 nm centered at 300 nm (region 1) and the broad absorption of 400–600 nm with peak at 532 nm (region 2) are indeed observed. Region 1 mainly results from the ligand to metal charge-transfer transitions and partly from the contribution of the Fe^{3+} ligand field transitions $^6A_1 \rightarrow {}^4T_1(4P)$ at 290–310 nm. Region 2 is assigned to the $^6A_1 + {}^6A_1 \rightarrow {}^4T_1(4G) + {}^4T_1(4G)$ excitation of an Fe^{3+}–Fe^{3+} pair, possibly overlapped the contributions of $^6A_1 \rightarrow {}^4E$, $^4A_1(4G)$ ligand field transition and the charge-transfer band tail [33,34]. In particular, the peak at 532 nm (2.33 eV) is related to the hematite optical band gap [20], an obvious blue shift than that of the bulk α-Fe_2O_3 (2.2 eV), which could be due to the well-known quantum size effect [36] resulted from the nanosize of α-Fe_2O_3 platelets. According to the quantum size effect, the nano-scaled semiconductor crystals keep the structural features of the bulk solid but the molecular orbitals should be discrete rather than continuous bands and higher irradiation energy is required to achieve electron excitations. Similar phenomena have been observed in cases of other metal oxides [37,38].

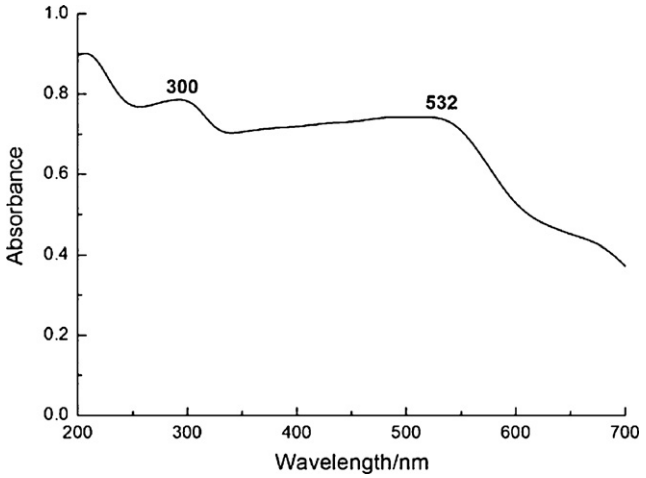

Fig. 6. UV–vis absorption spectra of α-Fe_2O_3 nanoplates.

4. Conclusions

To conclude, a facile PEG-600 assisted hydrothermal and post-heated route was developed to prepare quasi-hexagonal α-Fe_2O_3 nanoplates with lateral sizes of 40–60 nm and thickness of ca. 10 nm. The heat-treatment at a low temperature of 250 °C for a short period of 0.5 h presented little effect upon the morphology of final product. The formation and growth mechanism of α-Fe_2O_3 platelets under the assistance of PEG-600 was elucidated by a proposed adsorption-extension-attachment model. The α-Fe_2O_3 nanoplates exhibited a higher Langmuir surface area of 59 m^2/g and maximum N_2 adsorption of 137.3 cm^3/g compared with that of the mesoplates. UV–vis measurement showed a slight band gap blue-shift owing to the quantum size effect of the nanoplates. The

as-fabricated 2D α-Fe_2O_3 nanoplates could find potential applications in areas such as catalyst, gas sensor, or data storage.

Acknowledgements

This project was supported by the Education Commission of Tianjin (20090503) and National Natural Science Foundation of China (No. 20771083).

Appendix A. Supplementary data

Supplementary data associated with this article can be found, in the online version, at doi:10.1016/j.jallcom.2010.09.124.

References

[1] C. Burda, X. Chen, R. Narayanan, M.A. El-Sayed, Chem. Rev. 105 (2005) 1025–1102.
[2] S.W. Liu, J.G. Yu, M. Jaroniec, J. Am. Chem. Soc. 132 (2010) 11914–11916.
[3] J.K. Dongre, M. Ramrakhiani, J. Alloys Compd. 487 (2009) 653–658.
[4] C.Z. Wu, P. Yin, X. Zhu, C.Z. OuYang, Y. Xie, J. Phys. Chem. B 110 (2006) 17806–17812.
[5] X.L. Xie, H.Q. Yang, F.H. Zhang, L. Li, J.H. Ma, H. Jiao, J.Y. Zhang, J. Alloys Compd. 477 (2009) 90–99.
[6] M. Hermanek, R. Zboril, I. Medrik, J. Pechousek, C. Gregor, J. Am. Chem. Soc. 129 (2007) 10929–10936.
[7] S.K. Mohapatra, S.E. John, S. Banerjee, M. Misra, Chem. Mater. 21 (2009) 3048–3055.
[8] M. Srivastava, A.K. Ojha, S. Chaubey, J. Singh, P.K. Sharma, A.C. Pandey, J. Alloys Compd. 500 (2010) 206–210.
[9] C.H. Kim, H.J. Chun, D.S. Kim, S.Y. Kim, J. Park, J.Y. Moon, G. Lee, J. Yoon, Y. Jo, M.-H. Jung, S.I. Jung, C.J. Lee, Appl. Phys. Lett. 89 (2006) 223103-1–322103-3.
[10] A. Mao, G.Y. Han, J.H. Park, J. Mater. Chem. 20 (2010) 2247–2250.
[11] X.H. Liu, G.Z. Qiu, A.G. Yan, Z. Wang, X.G. Li, J. Alloys Compd. 433 (2007) 216–220.
[12] Z.H. Zhang, M.F. Hossain, T. Takahashi, Appl. Catal. B 95 (2010) 423–429.
[13] M.V. Reddy, T. Yu, C.H. Sow, Z.X. Shen, C.T. Lim, G.V. Subba Rao, B.V.R. Chowdari, Adv. Funct. Mater. 17 (2007) 2792–2799.
[14] S. Bharathi, D. Nataraj, M. Seetha, D. Mangalaraj, N. Ponpandian, Y. Masuda, K. Senthil, K. Yong, Cryst. Eng. Commun. 12 (2010) 373–382.
[15] G.X. Tong, J.G. Guan, W.H. Wu, L.C. Li, Y. Guan, Q. Hua, Sci. China Technol. Sci. 53 (2010) 1897–1903.
[16] L. Li, N. Koshizaki, J. Mater. Chem. 20 (2010) 2972–2978.
[17] S.B. Ni, S.M. Lin, Q.T. Pan, F. Yang, K. Huang, X.Y. Wang, D.Y. He, J. Alloys Compd. 478 (2009) 876–879.
[18] S.C. Yan, L.J. Wan, Z.S. Li, Y. Zhou, Z.G. Zou, Chem. Commun. 46 (2010) 6388–6390.
[19] W.Y. Yang, F.M. Gao, G.D. Wei, L.A. An, Cryst. Growth Des. 10 (2010) 29–31.
[20] J.J. Zhang, Y.Z. Cheng, Q. Yang, Mater. Lett. 63 (2009) 2075–2077.
[21] J.B. Wu, H. Zhang, N. Du, X.Y. Ma, D.R. Yang, J. Phys. Chem. B 110 (2006) 11196–11198.
[22] L. Han, Z. Shan, D.H. Chen, X.J. Yu, P.Y. Yang, B. Tu, D.Y. Zhao, J. Colloid Interface Sci. 318 (2008) 315–321.
[23] R.G. Pearson, J. Chem. Educ. 45 (1968) 581–587.
[24] X.L. Hu, J.M. Gong, L.Z. Zhang, J.C. Yu, Adv. Mater. 20 (2008) 4845–4850.
[25] C.C. Luo, Y.H. Zhang, Y.G. Wang, J. Mol. Catal. A 229 (2005) 7–12.
[26] F. Xu, X. Zhang, Y. Xie, X.B. Tian, Y.Z. Li, J. Colloid Interface Sci. 260 (2003) 160–165.
[27] J.P. Ge, Y.X. Hu, M. Biasini, W.P. Beyermann, Y.D. Yin, Angew. Chem. Int. Ed. 46 (2007) 4342–4345.
[28] Q. Zhang, S.J. Liu, S.H. Yu, J. Mater. Chem. 19 (2009) 191–207.
[29] R.A. Nyquist, R.O. Kagel, Infrared Spectra of Inorganic Compounds, Academic Press, New York, London, 1971, pp. 220.
[30] M. Žic, M. Ristić, S. Musić, J. Alloys Compd. 466 (2008) 498–506.
[31] A. Bernson, G. Lindgren, W. Huang, R. Frech, Polymer 36 (1995) 4471–4478.
[32] Y.Y. Xu, D.R. Chen, X.L. Jiao, K.Y. Xue, J. Phys. Chem. C 111 (2007) 16284–16289.
[33] Y.P. He, Y.M. Miao, C.R. Li, S.Q. Wang, L. Cao, S.S. Xie, G.Z. Yang, B.S. Zou, Phys. Rev. B 71 (2005) 125411–125419.
[34] D.M. Sherman, T.D. Waite, Am. Miner. 70 (1985) 1262–1269.
[35] M.F. Chioncel, C. Díaz-Guerra, J. Piqueras, J. Appl. Phys. 104 (2008) 124311-1–1124311-8.
[36] L. Brus, J. Phys. Chem. 90 (1986) 2555–2560.
[37] A.I. Inamdar, A.C. Sonavane, S.K. Sharma, H. Im, P.S. Patil, J. Alloys Compd. 495 (2010) 76–81.
[38] Q.C. Zhang, Z.H. Yu, G. Li, Q.M. Ye, J.H. Lin, J. Alloys Compd. 477 (2009) 81–84.